Download is permitted to HPC-Lab members and for educational purposes only

Powder Technology 336 (2018) 282–297

Contents lists available at ScienceDirect

Powder Technology

journal homepage: www.elsevier.com/locate/powtec

2D simulation of breakage of angular particles using combined DEM and XFEM

Javad Raisianzadeh, Ali Asghar Mirghasemi *, Soheil Mohammadi

School of Civil Engineering, College of Engineering, University of Tehran, Tehran, Iran

ARTICLE INFO

Article history:
Received 27 January 2018
Received in revised form 21 May 2018
Accepted 4 June 2018
Available online 06 June 2018

Keywords:
Particle breakage
Rockfill
Discrete element method
Extended finite element method
Crack propagation

ABSTRACT

Particle breakage in two-dimensional angular rockfill material is simulated using a combined DEM and XFEM approach. In this approach, the interaction of particles is simulated by DEM and breakage analysis is carried out on each particle using XFEM. Simplifying assumptions for the breakage path are eliminated in this approach and the history of cracking is considered for each particle in the breakage analysis. Simulation of various laboratory tests on rock samples and biaxial tests on rockfill assemblies show the ability of the proposed model to capture different aspects of particle breakage and the behavior of granular materials.

© 2018 Elsevier B.V. All rights reserved.

1. Introduction

Particle breakage greatly affects the mechanical behavior of granular materials. This phenomenon changes the grain size distribution curve and, consequently, alters the mechanical characteristics of granular materials. Particle breakage has been observed in soil-rockfill masses such as earthen dams, sub-bases of railroad tracks and in activities such as driving of large-displacement piles and conventional geotechnical investigation tests.

Several experimental studies have investigated the effects of particle breakage on the behavior of granular materials [1–8]. Marsal [1] studied the behavior of rockfill material using a large-scale triaxial apparatus. He concluded that particle breakage greatly influenced the shear strength and compressibility of the granular materials. Varadarajan et al. [8] performed triaxial compression tests on rounded and angular rockfill materials and found that the particle breakage increased as the confining pressure grew. They also noticed that any enlargement in the particle size increased the breakage factor because it increased the force per contact. In addition to the size, the geometric shape of particles also affected the rate of breakage. Moreover, a greater extent of interlocking between angular particles caused dilative behavior under shear loading and increased the particle breakage. Other researchers have reported similar results [2–7].

Along with the laboratory tests, numerical studies have been used to simulate particle breakage in granular media. Due to the difficulties associated with experimental tests and their high cost for larger-sized particles such as rockfill, numerical modelings of granular material as discrete particles have been extensively applied using the discrete element method (DEM) [9–30]. In most of these models, simplifying assumptions have been applied to model particle breakage. Also, the crack propagation history has not been incorporated in simulation of breakage mechanisms. In the present study, the goal is to model particle breakage in a more realistic way by combining DEM and the extended finite element method (XFEM). For this purpose, the behavior of a 2D granular assembly composed of angular rockfill particles is investigated during biaxial compression test.

2. Brief review of recent particle breakage simulations

Robertson and Bolton [14] and McDowell and Harireche [15] studied particle breakage in a 3D assembly of sand by modeling each breakable particle as an agglomerate of bonded unbreakable spheres in a crystallographic array. For each bond between every two unbreakable spheres, the shear and vertical stiffness were defined. A bond was considered broken when the tensile or shear forces exceeded a designated value. The results of this study showed the proficiency of the proposed method in modeling sand behavior. However, application of this method was limited to materials such as sand, because replacing sharply angled materials as is found in rockfill with an agglomerate of rounded spheres would not be consistent. This method has been utilized in various studies on sand [16–20].

Hosseininia and Mirghasemi [21, 22] studied 2D breakage of angular particles. In their study, each intact and uncracked polygonal particle was replaced by a number of more finely connected polygonal sub-particles. If the bond between two sub-particles was broken, breakage

* Corresponding author.
E-mail address: aghasemi@ut.ac.ir (A.A. Mirghasemi).

https://doi.org/10.1016/j.powtec.2018.06.006
0032-5910/© 2018 Elsevier B.V. All rights reserved.

would occur. They investigated the effect of particle breakage on the microscopic and macroscopic behavior of granular assemblies by simulating a set of biaxial tests.

Bagherzadeh-Khalkhali [23] and Bagherzadeh-Khalkhali et al. [24, 25] incorporated a method that combined DEM and FEM to simulate breakage in 2D rockfill particles. The assembly of particles was simulated using DEM. Then the stress-strain analyses on all particles were performed using FEM assumed that the particles were intact and uncracked. If the introduced breakage criteria were satisfied, the breakage path was determined based on the stress distribution in the particle. In this method, there was no need to assume the breakage path from the beginning of the simulation. It could be obtained using the best fit line through the plastic elements in the particle.

Luo et al. [27] modeled breakage in 2D polygonal particles using the combined DEM and scaled boundary finite element method (SBFEM). The probable breakage path for each particle was determined using a method similar to that introduced by Bagherzadeh-Khalkhali et al. Instead of discretizing each particle into finite elements, as done in the combined finite-discrete element method, stress-strain analysis of each particle was performed using SBFEM on a single polygon.

Ma et al. [28–30] used the combined DEM and FEM approach to investigate breakage in 2D and 3D granular materials. For breakage modeling, zero-thickness cohesive interface elements (CIEs) were inserted at the boundaries between elements and a progressive damage model was used for each CIE. The crack in each particle propagated according to the failure of the CIEs and the breakage path formed along these interface elements. Because remeshing of the particles was not performed during simulation, the size of the elements should be small enough to provide acceptable accuracy for the predicted breakage path.

One major shortcoming of these studies has been that, at each step of numerical modeling, the previous history of cracking of particle has not been considered in crack and breakage analysis of the particle. As a result, even a cracked (but not broken) particle under previous loading stages is considered to be completely intact and without a crack in subsequent steps unless it is fully broken.

3. Particle breakage modeling

In the present study, the effects of particle breakage on the behavior of a 2D granular assembly consisting of angular rockfill materials are investigated. For this purpose, particle breakage during biaxial compression test is simulated by combining the DEM and XFEM.

FEM is a common and efficient numerical method used in engineering problems. However, the classic FEM has shortcomings in the modeling of crack propagation problems. The main weakness of FEM for solving general crack propagation problems is that the finite elements should conform to the crack geometry at any given instant, i.e. the crack should not pass through an element of the mesh. Consequently, it is necessary to change all or part of the finite element mesh at each time step. Moreover, with remeshing at each step, transfer of information between time steps becomes very difficult.

Fig. 1a demonstrates one of the most popular FEM-based approaches for crack modeling using singular elements. The crack is modeled geometrically among elements and singular finite elements are introduced in the FEM mesh to simulate singular fields at the tip of the crack. Clearly, the crack can only propagate along the boundaries of the elements unless a remeshing scheme is adopted for general non-conforming crack propagations [31, 32]. These shortcomings are eliminated in XFEM, while the benefits of FEM are preserved. In XFEM, the crack is modeled virtually by introducing a series of enrichment functions derived from the analytical solutions for the crack problem (Fig. 1b). In this method, there is no need to adapt the mesh to the crack propagation path and simulation of a general crack propagation path can be readily performed on a fixed mesh.

The method proposed in this study has two main stages. The first is simulation of the biaxial test on an assembly of angular rockfill material using a predefined number of DEM cycles (Fig. 2a). In the second stage, each particle is modeled separately using XFEM under contact loads from adjacent particles to determine the crack propagation path (Fig. 2b and c). If the propagated crack causes breakage, the initial particle is replaced by two new particles in accordance with the final breakage path (Fig. 2d). This procedure is iterated until the biaxial test is completed.

The proposed model eliminates the need for simplifying assumptions for the breakage path. Moreover, XFEM allows modeling of crack propagation in a conventional finite element mesh and transfers the crack information to the next step without the limitations of classic FEM. This makes it possible to carry out breakage analysis on cracked particles at each step using the crack path propagation in previous steps. This incorporates the history of cracking into the breakage analysis of particles, which enables the model to account for progressive reduction of strength of particle and its influence on potential subsequent breakage.

All particles in the present model are 2D convex polygons. The model can further be extended to various particle shapes by adding

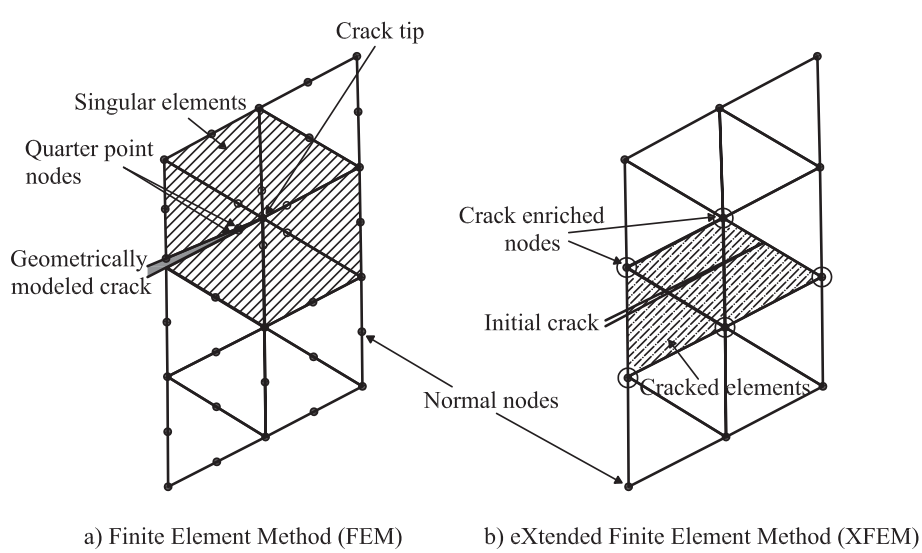

Fig. 1. Crack modeling methods: (a) FEM; (b) XFEM (adapted from Mohammadi [31, 32]).

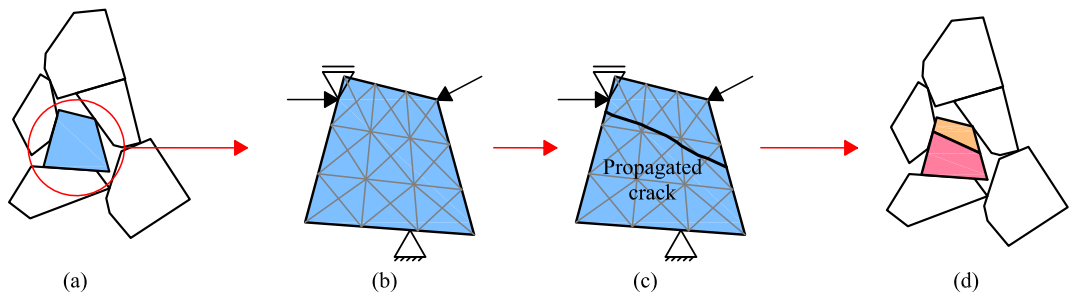

Fig. 2. Breakage modeling for a typical particle: (a) DEM model; (b) a typical discrete particle under exerted loads; (c) cracking of the particle; (d) breakage of the particle into two new discrete particles.

the ability of simulating 2D non-convex particles [33] in order to investigate particle breakage in a wider variety of materials. Also, by extending the model to 3D particles [29, 34], kinematics of particle fracture and rearrangement can be studied more accurately.

In the present research, a new DEM-XFEM code is developed for simulation of the particle-to-particle interaction and the breakage of every particle. The DEM part of the code is based on the program POLY, introduced by Mirghasemi et al. [35, 36]. Sections 3.1 and 3.2 briefly review the principles of DEM and XFEM. The proposed breakage model is presented in Section 3.3.

3.1. Simulation of particle assembly by DEM

DEM is a numerical method used for the simulation of the dynamic or pseudo-static interaction of an assembly of discrete elements. When a load is applied to a granular assembly, the forces acting on the boundaries are borne by the particles of that assembly. In fact, the boundary forces are transferred through contact between particles, i.e. the contact forces.

In DEM, the force exerted on each particle is the result of contact forces between that particle and adjacent particles. These forces are determined using a force-displacement law. Knowing the value of each contact force and calculating the resultant force acting on each particle allows the corresponding acceleration of each particle to be calculated using Newton's second law. By double integration of the acceleration over small time intervals, similar to the finite difference method, the new position of each particle can be determined. The time steps (Δt) are small enough so that the velocity and acceleration of the particles can be assumed to be constant over each time step.

The angular particles are convex in this study. Initially, the particles of the assembly are generated randomly in a circular area using a given particle size distribution and a specified number of particles. The generated particle assembly consists of limited types of polygonal particles. The number of each type of particle in the assembly is determined according to the particle size distribution and the total number of particles. Each type of particle is generated by constructing a convex polygon with a predefined number of edges inscribed in an arbitrary ellipse.

By assuming rigid particle behavior which is based on the fact that the deformation of particles is very small compared to the deformation of the assembly, it is possible to obtain the contact forces by calculating the area of overlap between two particles. These contact forces are considered to be external loads for XFEM analysis.

The geometric shape of the overlap area between two arbitrary rigid convex polygons is determined by finding the coordinates of the vertices of the area formed by the overlap between the two particles. The overlap area is then calculated using the coordinates of the vertices of the geometric shape. Two examples of overlap between two arbitrary particles are shown in Fig. 3.

In DEM, boundary conditions can be directly applied to the boundary particles in a granular assembly. In the method used in the present study, the particles are located in a circular area. To determine the boundary particles, it is assumed that a hypothetical rubber ring encompasses the particle assembly, as shown in Fig. 4. The particles in contact with this ring are recognized as the boundary particles. The boundary of the assembly is determined as a convex polygon connecting centers of the boundary particles to each other. Loadings can be applied to the boundary particles in both the strain-controlled and the stress-controlled conditions. In both cases, the velocity of the boundary particles are adjusted according to the specified strain or stress. In other words, the specified strain or stress is established in the particle assembly by applying the proportionate velocity to the boundary particles.

3.2. Crack modeling by XFEM

In XFEM, two sets of enrichment functions are added to the standard FEM approximations. One set is associated with modeling of displacement discontinuity in cracked elements. This eliminates the need for the mesh to conform to the crack path and a fixed and unaltered mesh can be used in different steps. The second set of enrichment functions are specified for the singular stress field around the crack tip. They are extracted from the analytical solutions for the basic Westergard crack problem [31, 32]. The desired accuracy can be achieved with fewer elements in a computationally more efficient approach than with classic FEM [31, 32, 37–43].

While it is known that adding tip enrichment functions can generally improve the accuracy of the stress and displacement fields, for general multi-crack propagation and fragmentation problems, only the discontinuity enrichment function provides the required accuracy and avoids the computational costs of singular enrichment functions, which have little effect on the global response [41–43].

In the present XFEM modeling, approximation of the unknown displacement u has two parts, the conventional FEM solution and the enriched part:

$$u^h(x) = \sum_{\forall I} N_I(x) u_I + \sum_{J \in S_H} N_J(x)\left[H(f(x)) - H(f(x_J))\right] q_J \quad (1)$$

where x is an arbitrary point in the domain of the problem, N are the conventional FEM shape functions, u_I are the conventional degrees of

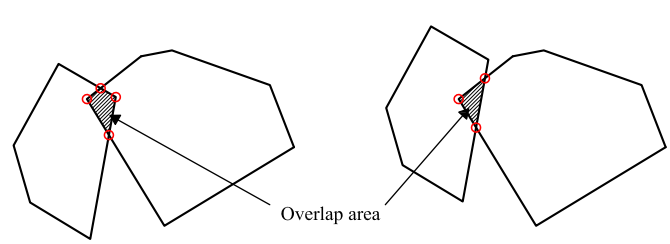

Fig. 3. Two typical cases of overlap between arbitrary particles.

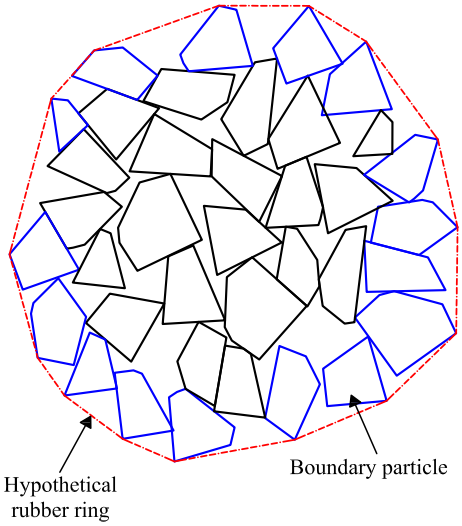

Fig. 4. Determination of boundary particles of the assembly.

freedom in FEM, q_J are the additional XFEM degrees of freedom and $H(f(x))$ is the discontinuity enrichment function. According to Eq. (1), the general solution for crack analysis in XFEM includes two parts. The first term corresponds to the conventional FEM solution and modeling discontinuity is enabled by incorporating the enrichment function into the second term. The second term corresponds to the nodes of elements located adjacent to the crack, which are denoted as S_H.

Existence of a displacement discontinuity across the crack is utilized by the Heaviside enrichment functions. A common definition of the Heaviside enrichment function is the sign function:

$$H(\xi) = sign(\xi) = \begin{cases} +1 & \forall \xi > 0 \\ -1 & \forall \xi < 0 \end{cases} \tag{2}$$

where ξ is the signed distance from the enriched node to the adjacent crack. For each node enriched by the Heaviside function, extra fictitious degrees of freedom are assigned with the same number and direction as the conventional degrees of freedom of that node. In this way, the discontinuity in displacement in both directions can be modeled.

With above definition for the discontinuity enrichment function, $f(x)$ and $f(x_J)$ in Eq. (1) are the signed distances from the arbitrary point x and the enriched node J to the adjacent crack, respectively. $H(f(x_J))$ is inserted in the enrichment term to shift the Heaviside function around the node of interest [31, 32]. In this case, the value of variable u on an enriched node k equals the real displacement of the node, satisfying the interpolation.

$$u^h(x_k) = u_k + [H(f(x_k)) - H(f(x_k))]q_k = u_k \tag{3}$$

XFEM analysis on each particle is repeated during the biaxial test due to the change in the boundary and loading conditions caused by the movement of particles in the assembly.

As stated before, considering numerous XFEM analyses under changing boundary and loading conditions [41–43], acceptable accuracy in the crack modeling along with avoiding excess computational efforts is achieved by just using the discontinuity enrichment functions. Using this solution for crack modeling implies that during each crack propagation step, the crack tip should be extended to reach the edge of the finite element that contains the crack tip. This assumption does not limit the propagation path of the crack. The crack propagates in only one element during each propagation step. This procedure is performed for all particles of the assembly. The cracked elements and enriched nodes are typically illustrated in Fig. 5 during propagation of an initial arbitrary crack.

Because of the polygonal shape of the particles, each particle is meshed using triangular elements. Due to the large number of particles, which create a large number of nodes in each XFEM analysis, the linear element (3-node element) is used to reduce the computational costs (Fig. 5).

The system of linear equilibrium equations in XFEM in its general form is written as [31, 32]:

$$\boldsymbol{K}\boldsymbol{u}^h = \boldsymbol{f} \tag{4}$$

where $\boldsymbol{K}$ is the stiffness matrix and $\boldsymbol{u}^h$ is the vector of degrees of freedom and includes both the conventional degrees of freedom and the extra fictitious degrees of freedom of the enriched nodes. The vector of the external forces is denoted by $\boldsymbol{f}$. The stiffness matrix and force vector of each element are assembled to compute the global stiffness matrix and force vectors. Stiffness matrix $\boldsymbol{k}^e$ and force vector $\boldsymbol{f}^e$ for each element e can be calculated as:

$$\boldsymbol{k}_{ij}^e = \begin{bmatrix} \boldsymbol{k}_{ij}^{uu} & \boldsymbol{k}_{ij}^{ua} \\ \boldsymbol{k}_{ij}^{au} & \boldsymbol{k}_{ij}^{aa} \end{bmatrix} \tag{5}$$

$$\boldsymbol{f}_i^e = \{\boldsymbol{f}_i^u \ \boldsymbol{f}_i^a\}^T \tag{6}$$

The vector of degrees of freedom for the nodes of each element $\boldsymbol{u}^h$ is defined as:

$$\boldsymbol{u}^h = \{\boldsymbol{u} \ \boldsymbol{a}\}^T \tag{7}$$

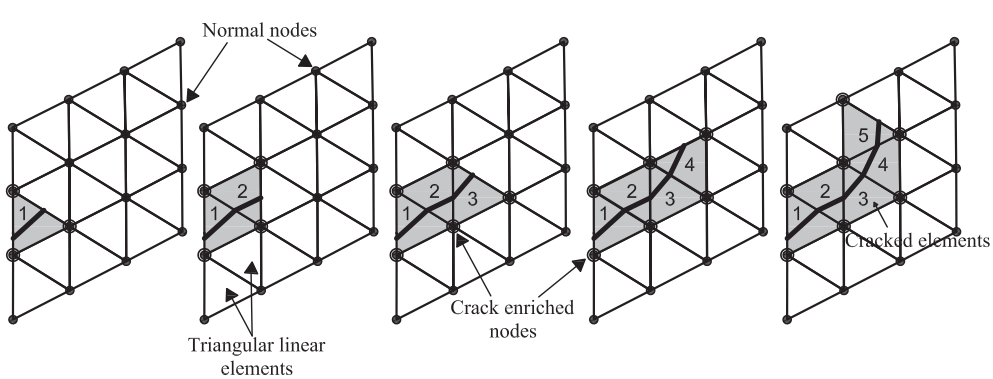

Fig. 5. Propagation of an arbitrary crack. The numbers correspond to the crack propagation steps.

where:

$$\boldsymbol{k}_{ij}^{rs} = \int_{\Omega^e} (\boldsymbol{B}_i^r)^T \boldsymbol{D} \boldsymbol{B}_j^s d\Omega, \qquad r, s = u, a \tag{8}$$

$$\boldsymbol{f}_i^u = \int_{\Gamma_t} N_i \boldsymbol{f}^t d\Gamma + \int_{\Omega^e} N_i \boldsymbol{f}^b d\Omega \tag{9}$$

$$\boldsymbol{f}_i^a = \int_{\Gamma_t} N_i H \boldsymbol{f}^t d\Gamma + \int_{\Omega^e} N_i H \boldsymbol{f}^b d\Omega \tag{10}$$

Γ_t is the traction boundary, Ω^e is the domain of element, $\boldsymbol{f}^t$ is the vector of external tractions acting on the boundaries and $\boldsymbol{f}^b$ is the vector of body forces. $\boldsymbol{B}$ in Eq. (8) is the matrix of shape function derivatives as:

$$\boldsymbol{B}_i^u = \begin{bmatrix} N_{i,\ x} & 0 \\ 0 & N_{i,\ y} \\ N_{i,\ y} & N_{i,\ x} \end{bmatrix} \tag{11}$$

$$\boldsymbol{B}_i^a = \begin{bmatrix} (N_i[H(\xi) - H(\xi_i)])_{,x} & 0 \\ 0 & (N_i[H(\xi) - H(\xi_i)])_{,y} \\ (N_i[H(\xi) - H(\xi_i)])_{,y} & (N_i[H(\xi) - H(\xi_i)])_{,x} \end{bmatrix} \tag{12}$$

The XFEM analysis is performed by assuming linear elastic material behavior. This is a valid assumption, as the considered rockfill material exhibits brittle behavior under compression loading.

3.3. Particle breakage analysis

Simulation of the biaxial test on the particle assembly is performed using DEM with very small time steps. At the beginning of the biaxial test, all particles are assumed to be intact and without cracks. During the biaxial test and between small time periods, breakage analysis is performed on all of the particles using XFEM. Due to the very small time steps of DEM analysis, particles movements are slight in each calculation cycle and cause negligible changes in the contact forces applied to the particles. Therefore, it is not required to conduct breakage analysis on the particles after each cycle of DEM. Each breakage analysis is performed following a predefined number of DEM analyses to reduce the computational costs. Sensitivity analysis is conducted to determine the sufficient number of DEM analyses for each breakage analysis (see Section 4).

After performing the determined number of DEM analyses, each particle is meshed independently. The boundary and loading conditions for each particle are determined according to the contacts of that particle with adjacent particles. If the particle has at least three contact points, two contact points are constrained to create a statically determinate system such that no instability occurs. The other contact points are considered to be external loading points. Fig. 6 shows the boundary conditions and external loads for two sample particles in the assembly. The amount of external loading is equal to the contact forces imposed on the particle.

XFEM stress-strain analysis is performed on each particle under the determined boundary and loading conditions. By obtaining the stress field in the particle, failure is controlled for every element based on the considered failure criterion. The first element to fail is assumed to be the crack initiation point. With initiation of the crack, XFEM analysis is carried out again on the particle and the generated stress field around the crack tip is controlled at local scale. If failure occurs in the neighborhood of the crack tip according to the failure criterion, the crack propagates in only one element along the angle specified by the failure criterion. XFEM analysis then is carried out again on the particle and the procedure is repeated. This computational loop continues until crack propagation in the particle stops (particle 1054 in Fig. 6) or results in breakage (particle 678 in Fig. 6). If the propagated crack reaches the particle boundaries, breakage occurs and the particle is divided into two new particles along the straight line connecting the start and end of the crack path. The properties of the two new particles are similar to that of the parent particle and they replace the parent particle in the assembly. After breakage analysis on all of the particles, DEM analysis of the updated assembly continues. This procedure is illustrated in Fig. 6 for two sample particles.

In the subsequent series of breakage analyses, the new particles formed by breakage in the previous series are meshed and analyzed under new boundary and loading conditions. Thus, the new particles could break again to produce finer particles.

The use of XFEM in the proposed model creates the ability to perform stress-strain analysis on the particles based on the propagated crack path. Thus, the history of crack propagation is accounted for in each step of breakage analysis.

There are certainly numerous microcracks in granular material, but during loading, these cracks eventually stop within the material or merge to form a main crack that may lead to breakage. Because this study focuses on breakage analysis rather than damage analysis, the microcracks are ignored in the numerical modeling and only the main crack, which creates the dominant failure mode of the material, is assumed in the analyses.

3.3.1. Criterion for initiation and propagation of crack

A rock failure criterion has been used to determine the crack initiation point and crack propagation path in the XFEM mesh. Various failure criteria have been presented for rocks. In this research, the Hoek-Brown criterion which is the most widely used criterion to predict the failure of any type of rock has been selected. The Hoek-Brown criterion for intact rock pieces is introduced as follows [44]:

$$\sigma_{1f} = \sigma_{3f} + \sigma_{ci}\left(m_i \frac{\sigma_{3f}}{\sigma_{ci}} + 1\right)^{0.5} \tag{13}$$

where m_i is a constant value which depends on the properties and type of rock, σ_{ci} is the uniaxial compressive strength of the rock and σ_{1f} and σ_{3f} are the major and minor principle stresses at failure, respectively. The value of m_i can be obtained by statistical analysis of the triaxial test results. If experimental test results are unavailable, m_i can be estimated using the values proposed by Hoek and Brown for different types of rock [44].

According to this criterion, the tensile strength is $\sigma_t = \frac{-\sigma_{ci}}{m_i}$. The elements in the particle which have a tensile stress greater than or equal to σ_t fail in tensile mode. The elements for which the major principle stress is greater than or equal to σ_{1f} fail in shear mode. The corresponding stress states are shown in Fig. 7a. The following safety factors have been defined to determine the failure of the finite element i [23–25]:

$$SF_i = \frac{\sigma_t}{\sigma_{3i}}; \text{Tensile failure} \tag{14}$$

$$SF_i = \frac{\sigma_{1f}}{\sigma_{1i}}; \text{Tensile failure} \tag{15}$$

where σ_{3i} and σ_{1i} are the minor and major principal stresses in element i, respectively, which are obtained from the XFEM stress-strain analysis of the particle. According to these equations, elements with safety factors smaller than 1 failed in the tensile or shear modes. The minor and major principle stresses of elements may exceed the failure stress that defined by the Hoek-Brown criterion because the stress-strain analyses are based on the linear elastic model.

Fig. 7a shows that the failure plane of the tensile mode is perpendicular to the tensile stress. According to the Hoek-Brown criterion, if failure occurs under the shear mode, the failure plane angle with respect to the major principle stress direction would be equal to $\beta = \pi/4 + \varphi/2$ which could be obtained easily from the Mohr circle construction shown in Fig. 7b. Thus, to determine the failure plane angle in shear

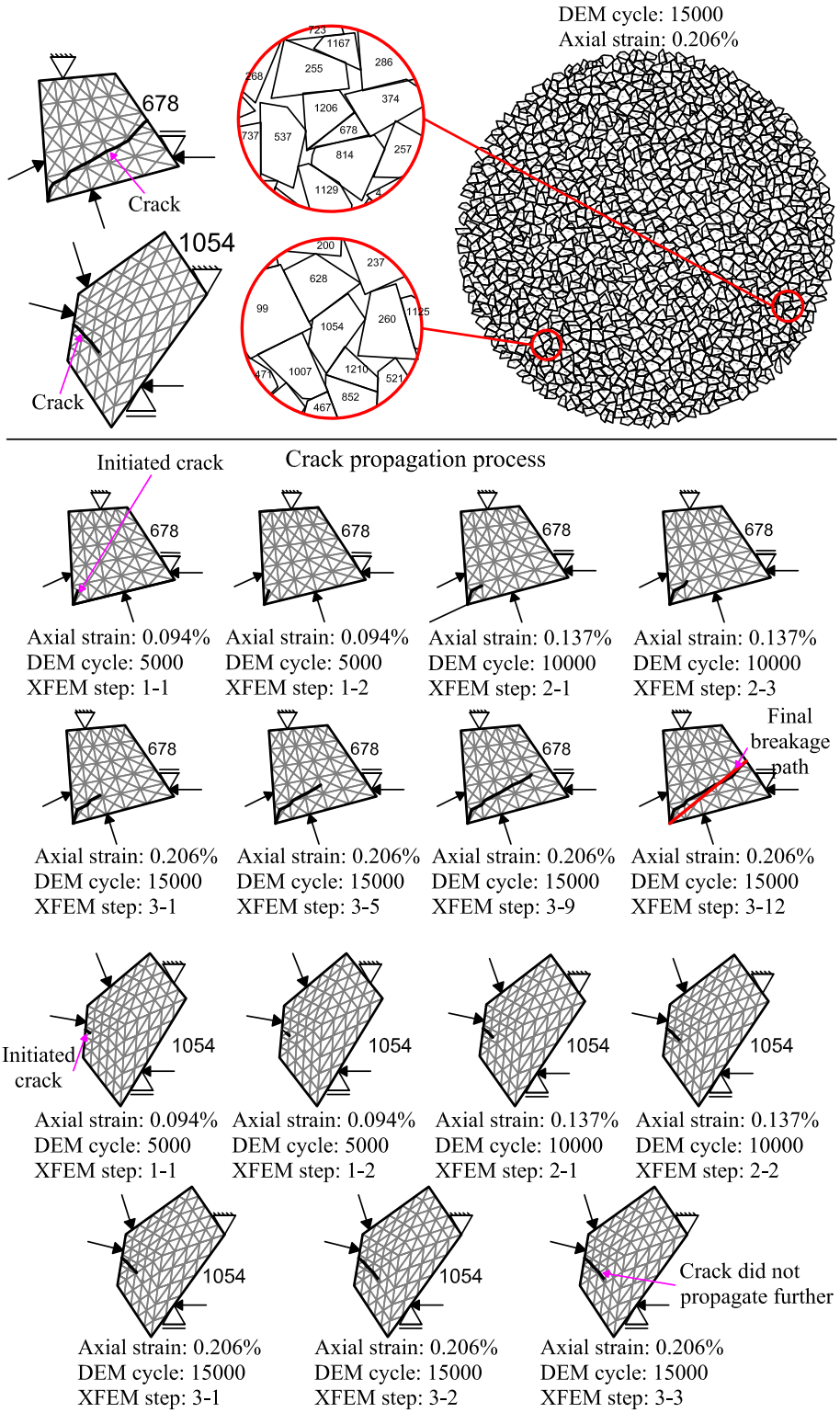

Fig. 6. Particle breakage analysis of two sample particles in the assembly.

mode, rock friction angle φ should be determined. Hoek et al. [46] fitted an average linear relationship to Eq. (13) and proposed the following expression to calculate ϕ using the parameters of the Hoek-Brown criterion:

$$\varphi = \sin^{-1}\left[\frac{6am_i\left(s+m_i\sigma'_{3n}\right)^{a-1}}{2(1+a)(2+a)+6am_i\left(s+m_i\sigma'_{3n}\right)^{a-1}}\right] \tag{16}$$

where a and s are the parameters of the generalized Hoek-Brown criterion and are equal to 0.5 and 1, respectively, for intact rock.

According to the procedure explained in Section 3.3, when the particle is intact, the first element that attains a safety factor smaller than 1 is assumed to be the crack initiation point. The crack angle is determined based on the type of failure mode (tensile or shear). For cracked particles, if the average stress around the crack tip produces a safety factor

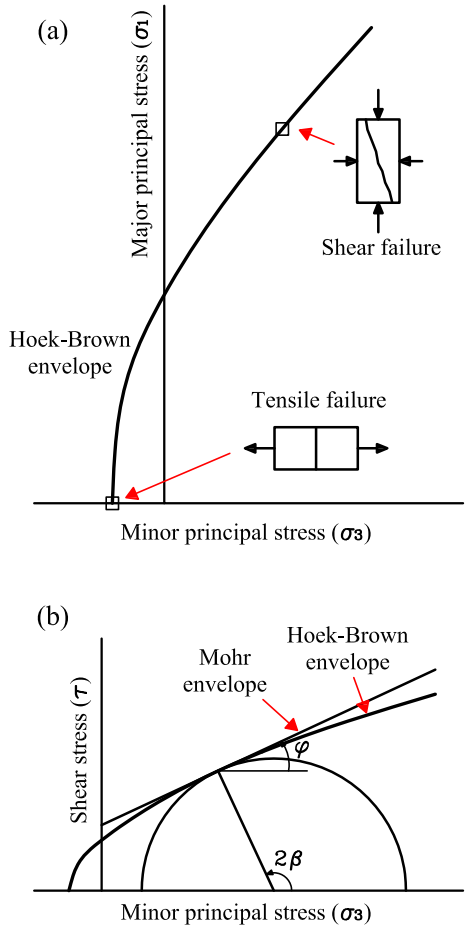

Fig. 7. (a) Stress states for tensile and shear failure modes; (b) Mohr circle and envelope for shear failure (adapted from Hoek [45]).

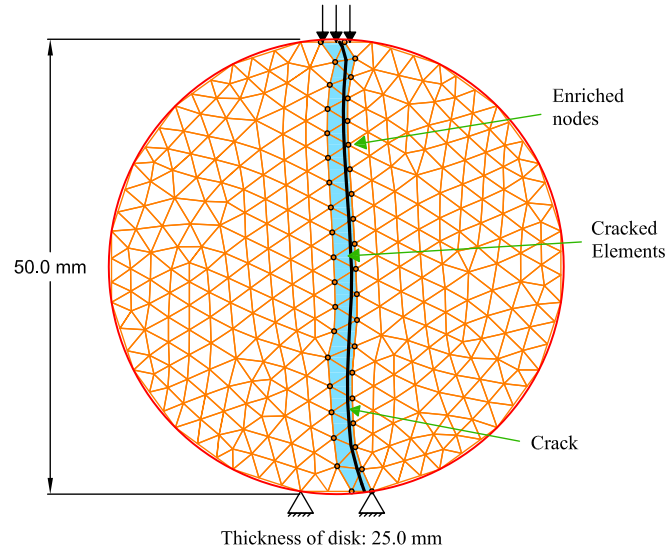

Fig. 8. Numerical simulation of the Brazilian test.

smaller than 1, the crack propagates along the tensile or shear failure plane.

3.4. Simulation of experimental tests on rock samples

A number of conventional laboratory tests on the intact rock, including the Brazilian, triaxial and uniaxial compression tests, were simulated to investigate the ability of the proposed model to simulate breakage. Given that the presented model is two-dimensional, the effects of three-dimensional conditions on the results were ignored.

The Brazilian or splitting tensile test is a simple test that is conducted on a disk specimen to measure the indirect tensile strength of rock [47, 48]. The Brazilian tests were simulated on intact disk specimens using XFEM. Because polygonal particles were used in the proposed model, the disk specimen for the Brazilian test was modeled as a regular 20-sided polygon to resemble the circular shape of the test specimen. The specimens were 100.0 mm in diameter with a thickness-to-diameter ratio of 0.5 according to ASTM D3967 [47].

Fig. 8 shows the propagated crack path in a simulated test specimen of sandstone. The cracked elements and the enriched nodes used for the crack simulation in XFEM can be seen. The crack propagated along the loading direction and the final breakage path divided the specimen into two halves. This is in agreement with the results of several experimental studies on homogeneous and isotropic intact rocks reported in the literature [48, 49].

Table 1 shows the results of the Brazilian tensile strength (BTS) and uniaxial compressive strength (UCS) reported for some types of rock as well as the results of BTS obtained by simulations. The figures listed in the table are the average of values reported in the literature [50]. This allows the scattered data from different geometrical conditions and preparation of samples in the laboratory tests to be included. The elasticity modulus, Poisson's ratio, uniaxial compressive strength and Hoek-Brown parameter (m_i) are required to be incorporated into the model. But in most studies on BTS of rock, the elasticity and Hoek-Brown parameters are not directly measured. In this case, m_i is selected based on the estimates suggested by Hoek and Brown for different types of rock [44]. In addition, the elasticity modulus is estimated from the UCS using the following relation based on Deere [51] and Palmström and Singh [52] for intact rock [53]:

$$E = MR \cdot \sigma_{ci} \tag{17}$$

where MR is the modulus ratio and can be determined according to rock type. Table 1 shows that there is a good agreement between the results of the numerical simulations and the experimental studies.

Table 1
Comparison of BTS results from numerical simulations in present study and experimental studies.

Rock type	Elasticity parameters		Hoek-Brown parameter (m_i)	Measured UCS (MPa) [50]	Measured BTS (MPa) [50]	BTS from numerical simulations (MPa)
	E (GPa)	Poisson's ratio				
Diorite	75.5	0.2	27.0	251.7	15.7	16.1
Granite	51.0	0.2	29.0	170.3	10.3	10.5
Limestone	38.5	0.25	12.0	76.9	6.0	6.4
Marble	30.0	0.25	10.0	10.1	10.1	9.7
Quartzite	51.0	0.23	18.0	172.0	13.0	13.1
Sandstone	20.0	0.24	13.0	105.3	9.5	9.6

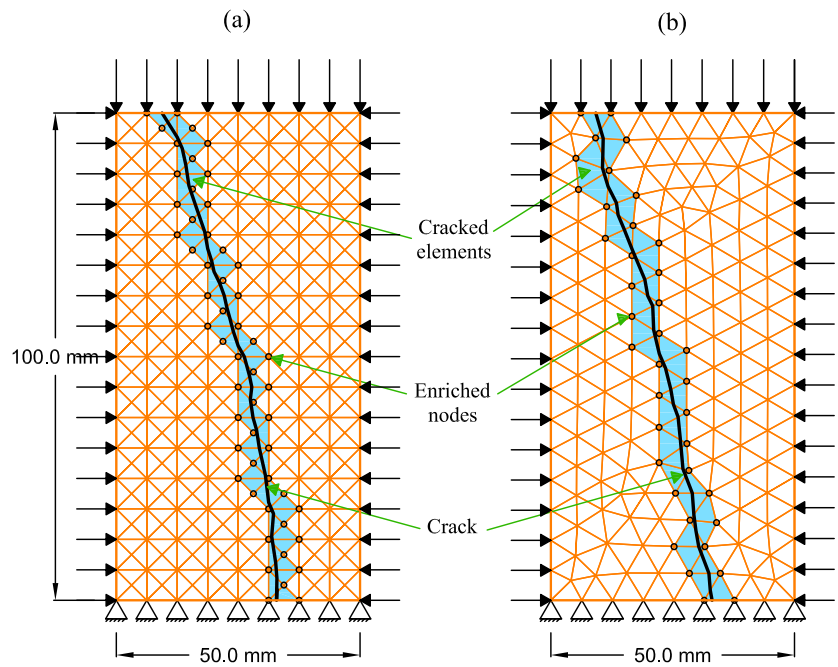

Fig. 9. Numerical simulation of the triaxial test using: (a) structured mesh; (b) unstructured mesh.

Fig. 9 shows the XFEM numerical model of a specimen under triaxial test with a confining pressure of 30 MPa using both structured and unstructured mesh. The specimens were assumed to be intact at the beginning of the test. The diameter and length-to-diameter ratio of the triaxial specimens were 50.0 mm and 2, respectively, which satisfied ASTM D7012 [54]. The cracked elements and the enriched nodes for crack simulation in XFEM are specified in Fig. 9. As seen, shear failure became the main mode of failure because of the laterally confined conditions. This is in agreement with the results of the experimental investigations carried out by Diederichs [55] on brittle rocks, which found that the shear failure became the main failure mode as the confining pressure increased.

Comparison of the results of numerical simulations using structured mesh and unstructured mesh showed that the proposed breakage model produced results that were similar independent of the type of mesh.

In another example, crack propagation was simulated in a sample with a pre-existing crack under uniaxial compression loading. Fig. 10a shows the crack inserted into the model before applying the load. Fig. 10b shows the crack path propagated under uniaxial loading which caused axial splitting of the sample. Several studies found that the primary mechanism of breakage under uniaxial loading was axial splitting, which occurred through initiation and propagation of wing cracks [56]. Wing cracks were initiated from both ends at an angle to the pre-existing crack and propagated in curvilinear form as the load increased [56]. These tensile cracks determined the breakage path under uniaxial loading and tended to be along the direction of loading [56]. As seen in Fig. 10, the results of the numerical simulation are in agreement with the experimental observations.

Overall, the examples demonstrate the efficiency of the proposed model for simulation of the crack and breakage in rock. An example is

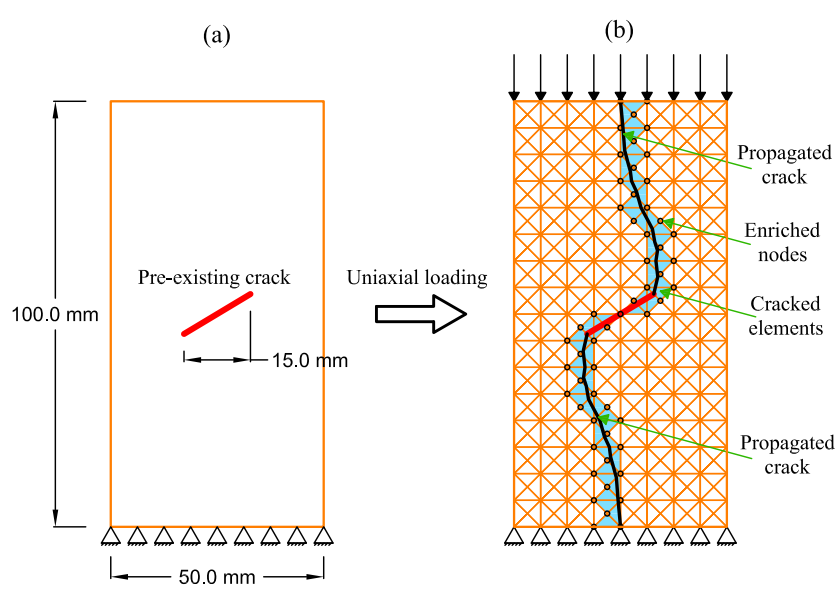

Fig. 10. Numerical simulation with a pre-existing crack under uniaxial compression loading: (a) specimen with the initial crack; (b) propagated crack under the uniaxial loading.

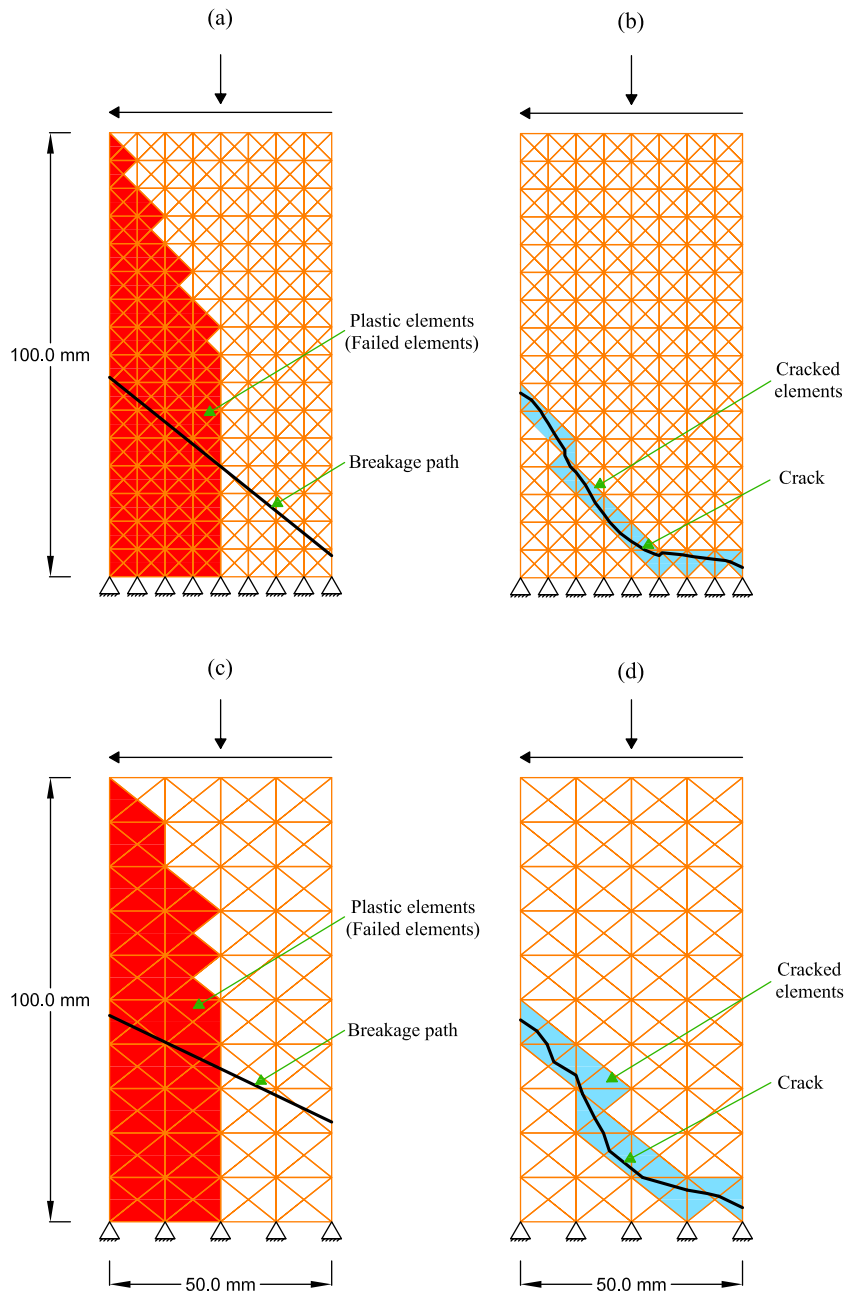

Fig. 11. Results of breakage analysis of a sample under simple shear loading (a) using the FEM [23] with fine mesh, (b) using the XFEM with fine mesh, (c) using the FEM [23] with coarse mesh, (d) using the XFEM with coarse mesh.

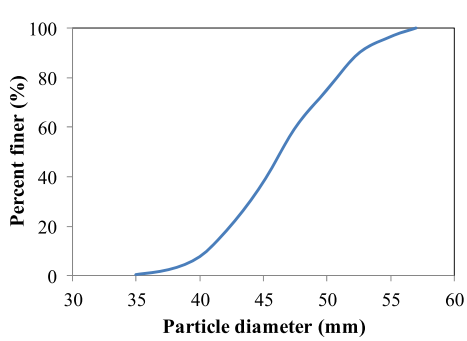

Fig. 12. Initial particle size distribution of the specimen.

presented here to compare the results of breakage simulation in rock using FEM [23–25] and XFEM. As discussed in Section 3.3, in the XFEM breakage analysis, the crack propagates in the particle based on the failure of cracked elements. If the propagated crack reaches the particle boundaries, breakage occurs. However, in the FEM approach used by Bagherzadeh-Khalkhali [23] and Bagherzadeh-Khalkhali et al. [24, 25], crack propagation is not modeled and the breakage is predicted based on the number of plastic elements (failed elements) in the particle along an average line passing through these elements. There must be a sufficient number of plastic elements to ensure reasonable accuracy in the predicted breakage path. Therefore, this method [23–25] requires a significant number of elements. An example was investigated to illustrate this issue. Fig. 11 shows a sample under simple shear loading where the breakage path was separately predicted using FEM (Fig. 11a and c) and XFEM (Fig. 11b and d) with fine and coarse finite element meshes. Clearly, because of the decreased number of plastic elements,

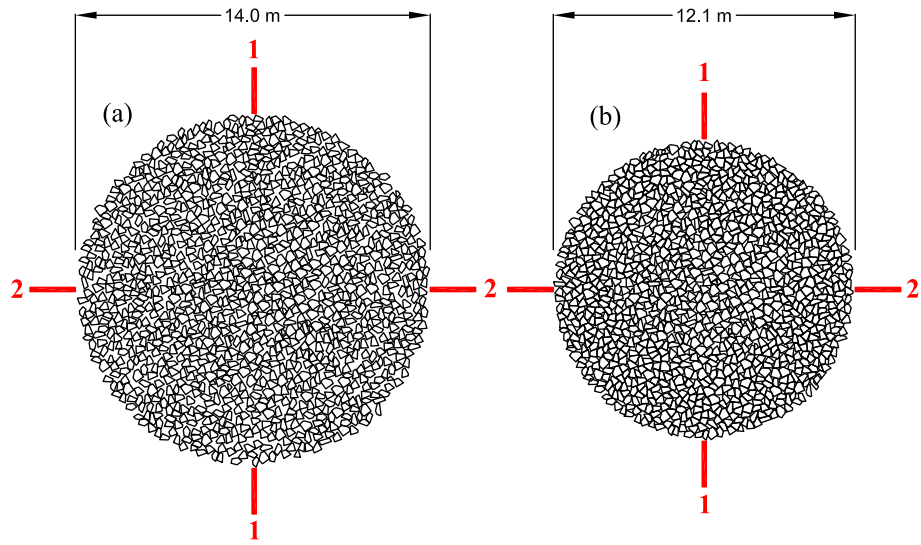

Fig. 13. (a) Initial generated assembly of particles; (b) specimen prepared under a confining pressure of 2 MPa prior to biaxial loading.

the breakage path predicted by FEM changed as the number of elements in the particle decreased. However, the propagated crack path of XFEM analysis remained unchanged despite the decrease in the number of elements, which shows the superior efficiency of the XFEM approach.

4. Simulation of biaxial tests

Simulations of the biaxial compression tests were performed in two groups. In one group of tests, breakage was disabled in the particles (BD) and in the other group, breakage was enabled (BE). The particle assembly included 1194 angular particles with a diameter of 35 to 57 cm. Fig. 12 shows the particle size distribution curve of the assembly. As in similar studies on 2D particles [26–28], the particle size in this study has been defined as the diameter of a circle that its area is equal to the area of the particle.

Each polygonal particle was meshed by 75 nodes and 120 elements on average, depending on its size and the number of edges, to obtain the required accuracy in the breakage analysis. Overall, in the assembly of particles, about 79,500 nodes and 130,700 elements were used for each XFEM analysis. Of course, these numbers increased as particle breakage occurred and new particles were meshed. The boundary particles were not allowed to be broken since their main role is to apply the boundary conditions.

Simulations of the biaxial tests were performed under drained conditions. First, the assembly of particles was created by randomly placing the particles in a circular area (Fig. 13a). Next, the initial loose assembly was compacted isotropically by applying a strain-controlled load to the boundary particles. After the required compaction was obtained, the particles were relaxed in their positions to reach a static state in which each particle had minimum contact with its neighboring particles.

In the next stage, the assembly was subjected to hydrostatic pressure by applying a stress-controlled load. This stage continued until the average internal stress of the particles reached the predetermined confining pressure and the volume (area in 2D) of the assembly reached a constant value. Fig. 13b shows the assembly of particles under a confining pressure of 2 MPa. Simulation of the bi-

Table 2
Parameters used in numerical simulations of biaxial testing.

Parameter		Value
Parameters used in the DEM analysis	Density of particles (kg/m^3)	2500
	Normal and tangential stiffness (N/m)	2×10^7
	Inter-particle friction coefficient	0.5
Parameters used in the breakage analysis	Elastic modulus (GPa)	20
	Poisson's ratio	0.2
	Uniaxial compressive strength (MPa)	150
	Hoek-Brown parameter, m_i	25.0

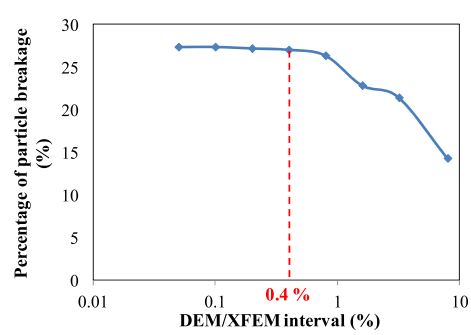

Fig. 14. Percentage of particle breakage for different DEM/XFEM analysis intervals at a confining pressure of 2 MPa.

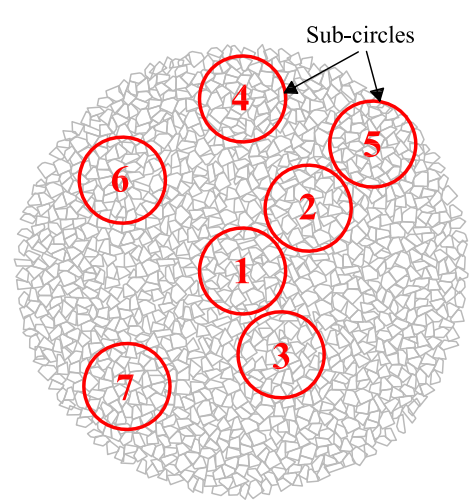

Fig. 15. Sub-circles in the assembly for comparison of deviatoric stress.

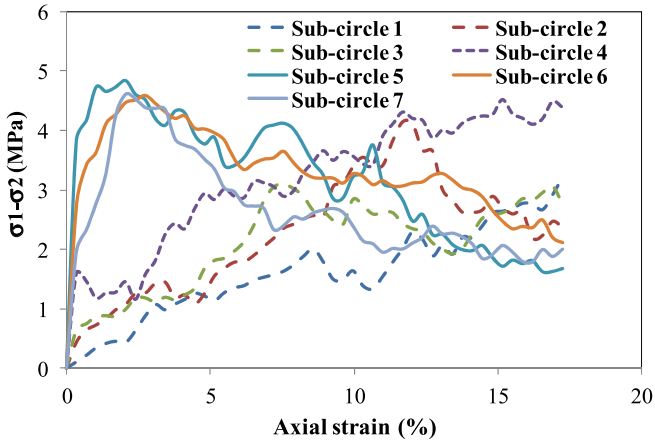

Fig. 16. Variation in deviatoric stress for different sub-circles versus axial strain of the whole particle assembly, during biaxial test with non-breakable particles under a confining pressure of 2 MPa.

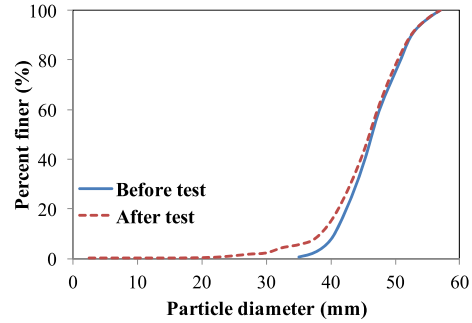

Fig. 18. Particle size distribution of breakable assembly at the beginning and end of biaxial test at a confining pressure of 2 MPa.

axial test was initiated through compression loading along the vertical direction (1–1) while the confining pressure was kept constant along the horizontal direction (2–2). Loading continued up to an axial strain of 16% to 18% in the different simulations. Loading was applied at a very small constant strain rate to establish quasi-static conditions during the test.

The simulations were performed under confining pressures of 0.5, 1, 2 and 4 MPa. Preparation of the specimens was such that all specimens had the same void ratio of $e = 0.3$ at the beginning of shear loading under different confining pressures.

Several parameters are required for numerical modeling using the combined DEM-XFEM method and determination of their accurate values requires performing various experimental tests. In the present research, these parameters were selected empirically because of the qualitative nature of the research. For comparison purposes, all parameters were assumed to be identical in the different simulations. The values used in this study are presented in Table 2.

As explained in Section 3.3, each breakage analysis using XFEM was performed after a specific number of DEM analyses. To determine the optimum number of DEM analyses for each XFEM analysis, several simulations were performed with different DEM/XFEM intervals and the effect of analysis interval on particle breakage was determined, as depicted in Fig. 14. A DEM/XFEM interval is the number of DEM cycles performed before each XFEM analysis normalized by the total number of DEM cycles of the biaxial test simulation (in percentage).

Fig. 14 shows the percentage of particle breakage during the biaxial tests with different DEM/XFEM intervals under a confining pressure of 2 MPa. The percentage of particle breakage increased as the DEM/XFEM intervals decreased. It reached to an approximately constant value when the DEM/XFEM interval became equal to or smaller than 0.4%. This indicates that a decrease in analysis intervals to <0.4% had a negligible effect on the particle breakage trend. In all simulations performed in this study, the DEM/XFEM analysis intervals were 0.4% to guarantee the accuracy of the simulations while reducing the computational costs.

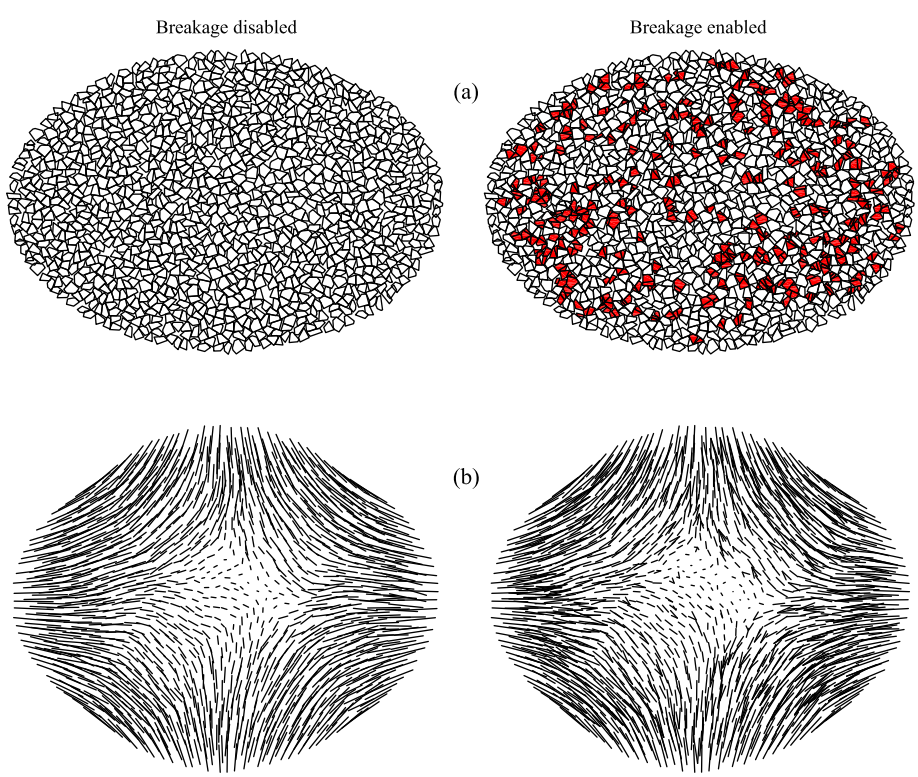

Fig. 17. (a) Assembly of particles; (b) displacement trajectories at the end of biaxial test at a confining pressure of 2 MPa.

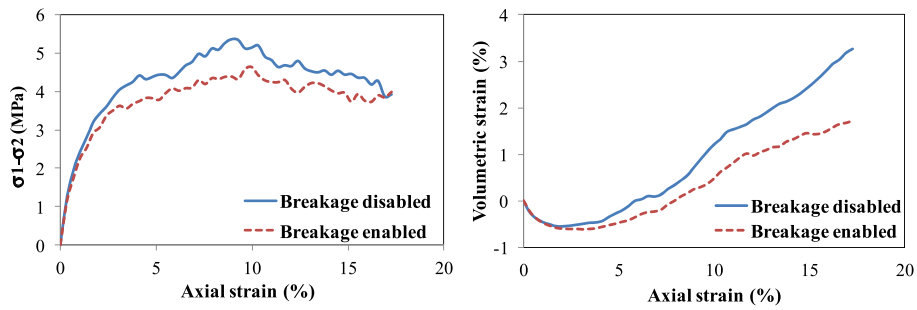

Fig. 19. Macroscopic results of biaxial test for breakable and non-breakable assemblies under a confining pressure of 2 MPa.

5. Results and discussion

5.1. Determination of RVE

In order to determine RVE, the deviatoric stress of sub-circles in the assembly was compared. As shown in Fig. 15, these sub-circles are located in different areas of the assembly and have the same diameter. Fig. 16 shows the variation in deviatoric stress for different sub-circles versus axial strain of the whole particle assembly, during biaxial test with non-breakable particles under a confining pressure of 2 MPa. Clearly, the deviatoric stress was lower for the inner sub-circles (1, 2 and 3) and showed an increasing trend during test. The stress was higher at sub-circle 4, which showed a trend similar to that of the inner sub-circles during test. For sub-circles 5, 6 and 7, after reaching a peak value in the initial stages of loading, the softening behavior caused the deviatoric stress to decrease significantly. It is evident that the stress is not similar in different areas of the assembly and it is not possible to determine an area which is representative of the behavior of the entire assembly. In other words, the whole particle assembly is considered as RVE in the present study.

5.2. Macroscopic behavior

Fig. 17 shows the assembly of particles and the displacement trajectories at the end of the biaxial test under a confining pressure of 2 MPa for the test groups having non-breakable (BD) and breakable (BE) particles. New particles created by particle breakage appear in red. The displacement trajectories that connect the initial and final positions of the particles indicate that the particles of the central area of the assembly showed less displacement. As expected, most breakage occurred in the areas with maximum relative displacement between adjacent particles. Comparison of the particle displacements of the BE and BD groups shows that the new particles created by breakage filled the void spaces between the existing particles and moved along with the adjacent particles.

Fig. 18 compares the particle size distributions of the breakable assembly at the beginning and end of the test under a confining pressure of 2 MPa. As seen, new particles with smaller diameters were created by the breakage of the larger particles, increasing the percentage of smaller particles and slightly reducing the average particle size of the specimen.

Fig. 19 shows the macroscopic behavior of the rockfill material during the biaxial test as curves of deviatoric stress and volumetric strain versus axial strain. The results were compared between groups BE and BD under a confining pressure of 2 MPa. As seen, the trends of shear strength and compressibility variation from the simulations are qualitatively in agreement with the results obtained from experimental studies [1, 8]. In both test groups BD and BE, the shear strength increased until reaching a peak value. Thereafter, it decreased gradually to a residual value at the end of the test. Moreover, the particle assembly showed a tendency towards a contractive behavior in the initial stages of loading, but the dilative behavior gradually dominated afterward.

Fig. 19 reveals that the shear strength of the assembly of breakable particles decreased compared to that of the non-breakable particles. It could be said that the shear strength of a granular assembly is a function of combined inter-particle friction and particle interlocking. Generally, increasing the interlocking between particles increases the shear strength. The same inter-particle friction coefficient was used in both series of BE and BD simulations. However, breakage in the BE test caused new particles, which were smaller than the parent particles, to fill the void spaces between particles, decreasing the interlocking. As seen, the decrease in void spaces and interlocking between particles reduced the dilative behavior in the breakable assembly.

Numerical simulations in this study have been performed on 2D particles. Because of the different kinematics of the particles and boundary conditions in 3D experimental tests such as triaxial compression, quantitative comparison of the numerical results with the experimental data is difficult. In order to compare the numerical results with the experimental data, the trend of the results as influenced by different parameters can be investigated. The maximum principal stress ratios (σ_1/σ_2) obtained from the numerical simulations of this study were compared with experimental data reported by various researchers [8] in Fig. 20. The numerical and experimental results are shown versus the breakage factor (B_g) as introduced by Marsal [1] and has been calculated from the grain size distributions of the sample. The breakage factor is defined as the sum of the decreases (or increases) in the percentage retained in the sieves after testing. As seen in Fig. 20, the numerical results are close to the lower bound of the experimental data, which indicates a good agreement between the numerical and experimental results. Moreover, a similar trend was observed in both the numerical and experimental results where the maximum principal stress ratio (σ_1/σ_2),

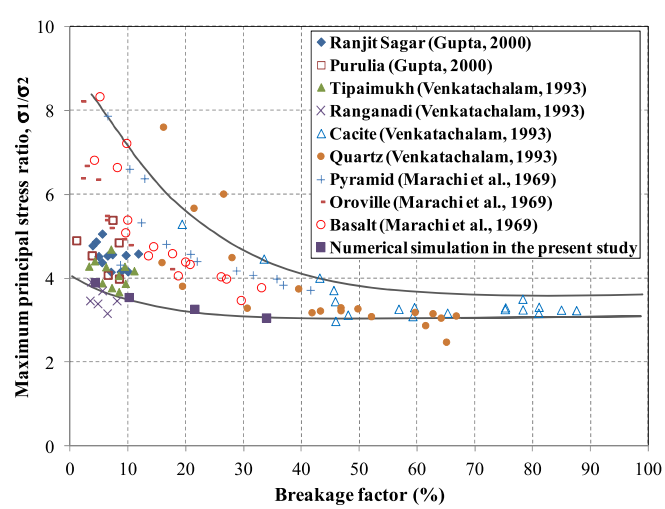

Fig. 20. Comparison of numerical results of the present study and experimental data reported by various researchers [8].

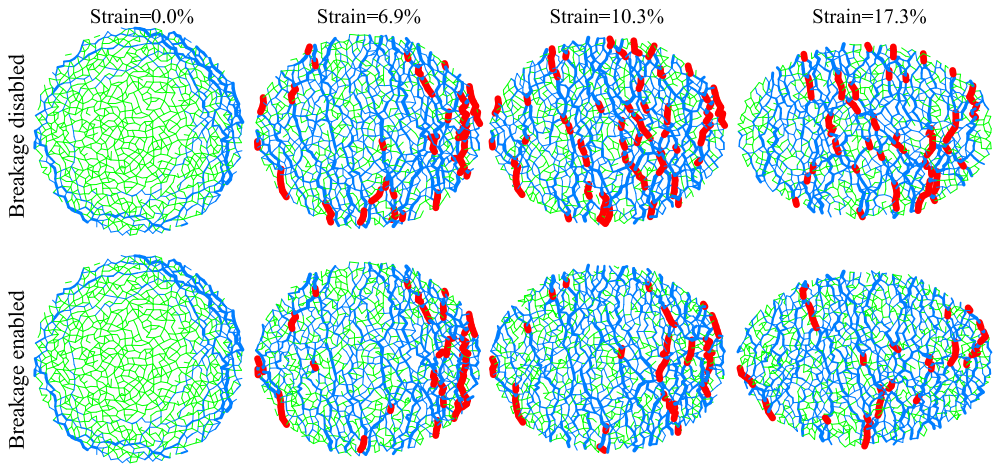

Fig. 21. Changes in normal contact force chains during biaxial test at a confining pressure of 2 MPa for breakable and non-breakable assemblies.

which indicates the strength of materials, decreased as the breakage factor increased.

5.3. Contact force chains

The effect of particle breakage on the behavior of the assembly was investigated at the microstructure level by comparing changes in the normal contact force chains during the biaxial test under a confining pressure of 2 MPa. Fig. 21 shows the results for the BE and BD simulations at three levels of force: weak ($F_N \leq 7$ kN; green lines), moderate (7 kN < $F_N \leq 50$ kN; blue lines) and strong (50 kN < F_N; red lines). For both groups, the contact forces increased during the biaxial test until reaching an axial strain of about 10%, which is equivalent to the peak shear strength. Thereafter, similar to the trend observed for shear strength, the contact forces gradually reduced. Furthermore, as the shear loading increased, the rather uniform distribution of weak contact

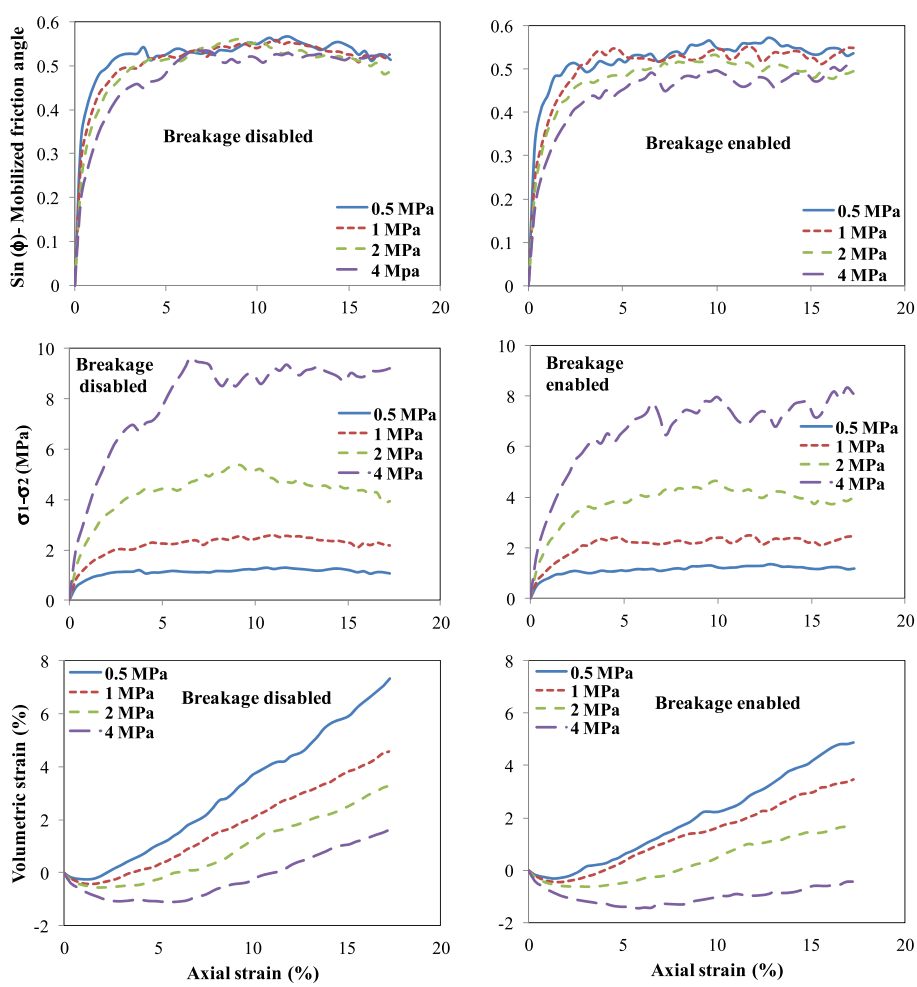

Fig. 22. Comparison of macroscopic results of biaxial test for breakable and non-breakable assemblies at different confining pressures.

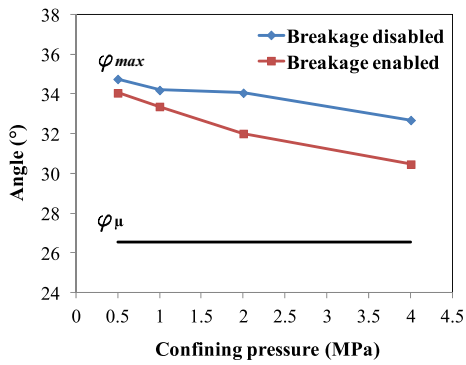

Fig. 23. Maximum mobilized friction angle and inter-particle friction angle at different confining pressures for breakable and non-breakable assemblies.

forces at the beginning of the test changed to a non-uniform distribution of moderate and strong contact forces at peak shear strength.

Comparison of the force chains between the BE and BD groups shows that the contact forces in the breakable assembly were more uniformly distributed and the number of strong forces decreased. This difference was more evident at higher strains, where the percentage of broken particles was greater. In fact, the strong contact forces resulted from the high amount of interlocking and stress concentration between particles. When breakage occurred, this interlocking was removed and the stress concentration was released. Therefore, increasing the number of breakages decreased the number of strong forces. This issue can also be explained by the fact that greater force per contact was produced between the larger particles [57]. Therefore, an increase in the number of finer particles caused by breakage reduced the magnitude of contact forces. This reduced concentration and more uniform distribution of contact forces was also observed by Luo et al. [27] and Tsoungui et al. [58], who referred to it as the "hydrostatic cushioning effect".

5.4. Effect of confining pressure on macroscopic behavior

Fig. 22 shows the mobilized friction angle, deviatoric stress and volumetric strain versus the axial strain at different confining pressures for the BE and BD simulations. The mobilized friction angle can be calculated as follows:

$$\varphi = \sin^{-1}\left(\frac{\sigma_1 - \sigma_2}{\sigma_1 + \sigma_2}\right) \tag{18}$$

where σ_1 and σ_2 are the average stresses of the particle assembly along the vertical and horizontal directions, respectively.

During the biaxial test, σ_2 was kept constant and equal to the confining pressure. For both series of simulations, as the confining pressure increased, the deviatoric stress or shear strength of assemblies increased. Also, the shear stresses gradually approached a steady value at the residual shear strength. As shown, the mobilized friction angle increased at lower confining stresses owing to greater dilation. These results are in agreement with the trends observed in experimental studies [1, 8]. Particle breakage intensified the influences of confining pressure on the mobilized friction angle and volume change behavior of the simulated samples. In other words, increasing the confining pressure led to more reduction in the mobilized friction angle and dilative behavior due to particle breakage in BE simulations.

Fig. 23 shows maximum mobilized friction angle φ_{max} at different confining pressures for the BE and BD simulations. Inter-particle friction angle φ_{μ} was the same for all simulations. In both the breakable and non-breakable assemblies, φ_{max} decreased with an increase in the confining pressure. Particle breakage caused the value of φ_{max} to decrease more in the breakable assembly. It can be concluded that such a phenomenon was the result of the simultaneous effect of particle breakage and confining pressure on the shear strength of the simulated materials in the breakable assemblies. The values of φ_{max} for the breakable and non-breakable assemblies were close at the low confining pressures due to a lower percentage of particle breakage. These results indicate that the main factor which reduced the maximum friction angle of rockfill material at higher confining pressures was the particle breakage.

5.5. Cracking and breakage of particles

Fig. 24 shows the variation in the percentage of particle breakage and number of cracked particles during the biaxial test at different confining pressures. As shown, the rate of particle cracking increased rapidly in the initial stages and then decreased as the axial strain increased. Particle breakage increased at an almost constant rate during the test. As discussed in Section 3.3, crack initiation in a particle did not necessarily result in breakage, although each cracked particle was analyzed in the next step to investigate the potential propagation of the existing crack. The steady rate of particle breakage gradually increased the number of broken particles, which decreased the interlocking and stress concentration between the particles and, consequently, decreased the rate of cracking in the remaining particles.

6. Summary and conclusions

The present study simulated particle breakage in 2D angular rockfill material using an approach that combines DEM and XFEM. In this approach, the interaction of particles is simulated by DEM and the breakage analysis is performed on each particle using XFEM under the contact forces of the adjacent particles derived from the DEM analysis. The proposed model eliminates the need for simplifying assumptions for the breakage simulation.

Simulations of various laboratory tests on rock samples showed the ability of the proposed model to accurately predict the crack propagation path and failure strength of rock. Simulations of the biaxial tests were performed at different confining pressures for breakable and non-breakable particle groups. The macroscopic behavior of the particle

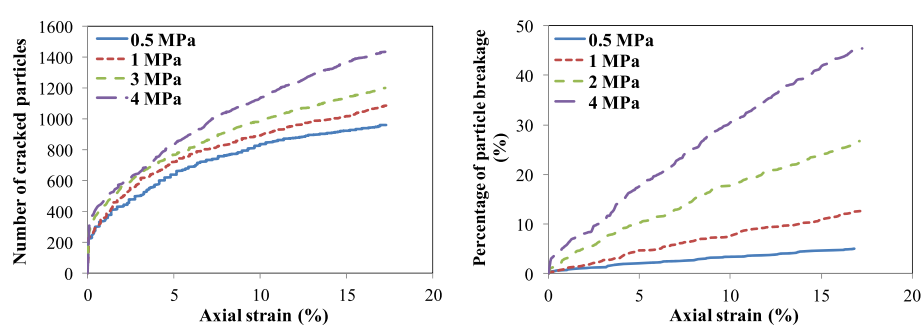

Fig. 24. Variation in number of cracked particles and percentage of particle breakage during biaxial test at different confining pressures.

assembly was qualitatively in agreement with the results of experimental studies [1, 8]. The major findings were:

- The confinement conditions significantly changed the failure mode of the material, which was captured by the proposed XFEM breakage model, as was observed in the experimental studies.
- Particle breakage caused a decrease in the number of strong contact forces and a more uniform distribution of contact forces by removing the interlocking between particles and releasing the stress concentrations.
- An increase in confining pressure reduced the internal friction angle and dilative behavior of the particle assembly. Particle breakage, which increased at higher confining pressures, intensified these effects.
- Particle cracking increased rapidly in the initial stages of loading and then decreased as the axial strain increased. Particle breakage increased at an almost constant rate during the test. Crack initiation in a particle did not necessarily result in breakage.

Generally, the results of the simulations showed the ability of the proposed model to capture different aspects of particle breakage and granular materials behavior.

Acknowledgements

This work was technically supported by the High Performance Computing Lab, University of Tehran.

References

[1] R.J. Marsal, Large-scale testing of rockfill materials, Journal of the Soil Mechanics and Foundations Division. 93 (2) (1967 Mar 2) 27–43.
[2] N.D. Marachi, C.K. Chan, H.B. Seed, Evaluation of properties of rockfill materials, Journal of Soil Mechanics & Foundations Div. 97 (SM1) (1971 Jan 1) 95–114.
[3] J.A. Charles, K.S. Watts, The influence of confining pressure on the shear strength of compacted rockfill, Geotechnique 30 (4) (1980 Dec) 353–367.
[4] B.O. Hardin, Crushing of soil particles, J. Geotech. Eng. 111 (10) (1985 Oct) 1177–1192.
[5] P.V. Lade, J.A. Yamamuro, Undrained sand behavior in axisymmetric tests at high pressures, J. Geotech. Eng. 122 (2) (1996 Feb) 120–129.
[6] J.A. Yamamuro, P.V. Lade, Drained sand behavior in axisymmetric tests at high pressures, J. Geotech. Eng. 122 (2) (1996 Feb) 109–119.
[7] P.V. Lade, J.A. Yamamuro, P.A. Bopp, Significance of particle crushing in granular materials, J. Geotech. Eng. 122 (4) (1996 Apr) 309–316.
[8] A. Varadarajan, K.G. Sharma, K. Venkatachalam, A.K. Gupta, Testing and modeling two rockfill materials, J. Geotech. Geoenviron. 129 (3) (2003 Mar) 206–218.
[9] P.A. Cundall, O.D. Strack, A discrete numerical model for granular assemblies, Geotechnique 29 (1) (1979 Mar) 47–65.
[10] F. Kun, H.J. Herrmann, A study of fragmentation processes using a discrete element method, Comput. Methods Appl. Mech. Eng. 138 (1–4) (1996 Dec 1) 3–18.
[11] A.V. Potapov, C.S. Campbell, Computer simulation of impact-induced particle breakage, Powder Technol. 81 (3) (1994 Dec 1) 207–216.
[12] A.V. Potapov, C.S. Campbell, Parametric dependence of particle breakage mechanisms, Powder Technol. 120 (3) (2001 Oct 22) 164–174.
[13] B. Sheikh, A. Pak, Numerical investigation of the effects of porosity and tortuosity on soil permeability using coupled three-dimensional discrete-element method and lattice Boltzmann method, Phys. Rev. E 91 (5) (2015 May 11) 053301-1–053301-14.
[14] D. Robertson, M.D. Bolton, DEM Simulations of Crushable Grains and Soils. Powders and Grains, Vol. 1, 2001 May 25.
[15] G.R. McDowell, O. Harireche, Discrete element modelling of soil particle fracture, Geotechnique 52 (2) (2002 Mar 1) 131–135.
[16] Y.P. Cheng, M.D. Bolton, Y. Nakata, Crushing and plastic deformation of soils simulated using DEM, Geotechnique 54 (2) (2004 Mar) 131–141.
[17] M.D. Bolton, Y. Nakata, Y.P. Cheng, Micro-and macro-mechanical behaviour of DEM crushable materials, Geotechnique 58 (6) (2008 Aug 1) 471–480.
[18] G.R. McDowell, J.P. de Bono, On the micro mechanics of one-dimensional normal compression, Geotechnique 63 (11) (2013 Jul 21) 895–908.
[19] J.P. de Bono, G.R. McDowell, DEM of triaxial tests on crushable sand, Granul. Matter 16 (4) (2014 Aug 1) 551–562.
[20] J.P. de Bono, G.R. McDowell, Particle breakage criteria in discrete-element modelling, Geotechnique 66 (12) (2016 Jul 4) 1014–1027.
[21] E.S. Hosseininia, A.A. Mirghasemi, Numerical simulation of breakage of two-dimensional polygon-shaped particles using discrete element method, Powder Technol. 166 (2) (2006 Aug 21) 100–112.
[22] E.S. Hosseininia, A.A. Mirghasemi, Effect of particle breakage on the behavior of simulated angular particle assemblies, China Particuology. 5 (5) (2007 Oct 31) 328–336.
[23] Bagherzadeh-Khalkhali, A. Numerical simulation of particle breakage in rockfill using combined DEM and FEM, University of Tehran, Iran, 2008.
[24] A. Bagherzadeh-Khalkhali, A.A. Mirghasemi, S. Mohammadi, Micromechanics of breakage in sharp-edge particles using combined DEM and FEM, Particuology. 6 (5) (2008 Oct 31) 347–361.
[25] A. Bagherzadeh-Khalkhali, A.A. Mirghasemi, S. Mohammadi, Numerical simulation of particle breakage of angular particles using combined DEM and FEM, Powder Technol. 205 (1) (2011 Jan 10) 15–29.
[26]] Xu W, Xu B, Guo F, Elastic properties of particle-reinforced composites containing nonspherical particles of high packing density and interphase: DEM–FEM simulation and micromechanical theory, Comput. Methods Appl. Mech. Eng. 326 (2017 Nov 1) 122–143.
[27] T. Luo, E.T. Ooi, A.H. Chan, S.J. Fu, The combined scaled boundary finite-discrete element method: grain breakage modelling in cohesion-less granular media, Comput. Geotech. 88 (2017 Aug 31) 199–221.
[28] G. Ma, W. Zhou, X.L. Chang, Modeling the particle breakage of rockfill materials with the cohesive crack model, Comput. Geotech. 61 (2014 Sep 30) 132–143.
[29] G. Ma, W. Zhou, X.L. Chang, M.X. Chen, A Hybrid Approach for Modeling of Breakable Granular Materials Using Combined Finite-Discrete Element Method. Granular Matter, 2016 Feb 1;18(1 7.
[30] G. Ma, W. Zhou, R.A. Regueiro, Q. Wang, X. Chang, Modeling the fragmentation of rock grains using computed tomography and combined FDEM, Powder Technol. 308 (2017 Feb 15) 388–397.
[31] S. Mohammadi, Extended Finite Element Method: For Fracture Analysis of Structures, Blackwell Publishing, Oxford, 2008.
[32] Mohammadi S. XFEM fracture analysis of composites, United Kingdom: John Wiley & Sons, 2012.
[33] W. Xu, Z. Han, L. Tao, Q. Ding, H. Ma, Random non-convex particle model for the fraction of interfacial transition zones (ITZs) in fully-graded concrete, Powder Technol. 323 (2018 Jan 1) 301–309.
[34] H. Ma, W. Xu, Y. Li, Random aggregate model for mesoscopic structures and mechanical analysis of fully-graded concrete, Comput. Struct. 177 (2016 Dec 1) 103–113.
[35] A.A. Mirghasemi, L. Rothenburg, E.L. Matyas, Numerical simulations of assemblies of two-dimensional polygon-shaped particles and effects of confining pressure on shear strength, Soils Found. 37 (3) (1997 Sep 15) 43–52.
[36] A.A. Mirghasemi, L. Rothenburg, E.L. Matyas, Influence of particle shape on engineering properties of assemblies of two-dimensional polygon-shaped particles, Geotechnique 52 (3) (2002 Apr) 209–217.
[37] J. Dolbow, N. Moës, T. Belytschko, An extended finite element method for modeling crack growth with frictional contact, Comput. Methods Appl. Mech. Eng. 190 (51–52) (2001 Oct 26) 6825–6846.
[38] T.P. Fries, T. Belytschko, The intrinsic XFEM: a method for arbitrary discontinuities without additional unknowns, Int. J. Numer. Methods Eng. 68 (13) (2006 Dec 24) 1358–1385.
[39] S. Bordas, S. Natarajan, P. Kerfriden, C.E. Augarde, D.R. Mahapatra, T. Rabczuk, S.D. Pont, On the performance of strain smoothing for quadratic and enriched finite element approximations (XFEM/GFEM/PUFEM), Int. J. Numer. Methods Eng. 86 (4–5) (2011 Apr 29) 637–666.
[40] R. Rashetnia, S. Mohammadi, Finite strain fracture analysis using the extended finite element method with new set of enrichment functions, Int. J. Numer. Methods Eng. 102 (6) (2015 May 11) 1316–1351.
[41] A. Daneshyar, S. Mohammadi, Strong tangential discontinuity modeling of shear bands using the extended finite element method, Comput. Mech. 52 (5) (2013 Nov 1) 1023–1038.
[42] M. Eftekhari, S.H. Ardakani, S. Mohammadi, An XFEM multiscale approach for fracture analysis of carbon nanotube reinforced concrete, Theor. Appl. Fract. Mech. 72 (2014 Aug 31) 64–75.
[43] E. Goli, H. Bayesteh, S. Mohammadi, Mixed mode fracture analysis of adiabatic cracks in homogeneous and non-homogeneous materials in the framework of partition of unity and the path-independent interaction integral, Eng. Fract. Mech. 131 (2014 Nov 30) 100–127.
[44] E. Hoek, E.T. Brown, Practical estimates of rock mass strength, Int. J. Rock Mech. Min. Sci. 34 (8) (1997 Dec 1) 1165–1186.
[45] E. Hoek, Strength of jointed rock masses, Geotechnique 33 (3) (1983 Sep) 187–223.
[46] Hoek E, Carranza-Torres C, Corkum B. Hoek-Brown Failure Criterion-2002 Edition. Proceedings of NARMS-Tac. 2002 Jul 7;1:267–73.
[47] A.S.T.M.D. 3967-08, Standard Test Method for Splitting Tensile Strength of Intact Rock Core Specimens. ASTM International, West Conshohocken, USA, 2008.
[48] D. Li, L.N. Wong, The Brazilian disc test for rock mechanics applications: review and new insights, Rock Mech. Rock. Eng. 46 (2) (2013 Mar 1) 269–287.
[49] M. Mellor, I. Hawkes, Measurement of tensile strength by diametral compression of discs and annuli, Eng. Geol. 5 (3) (1971 Oct 1) 173–225.
[50] M.A. Perras, M.S. Diederichs, A review of the tensile strength of rock: concepts and testing, Geotech. Geol. Eng. 32 (2) (2014 Apr 1) 525–546.
[51] D.U. Deere, Chapter 1: Geological Considerations, in: K.G. Stagg, O.C. Zienkiewicz (Eds.), Rock Mechanics in Engineering Practice, John Wiley and Sons, London 1968, pp. 1–20.
[52] A. Palmström, R. Singh, The deformation modulus of rock masses—comparisons between in situ tests and indirect estimates, Tunn. Undergr. Space Technol. 16 (2) (2001 Apr 30) 115–131.
[53] E. Hoek, Practical Rock Engineering, Available online http://www.rockscience.com 2000.
[54] A.S.T.M.D. 7012, Standard Test Method for Compressive Strength and Elastic Moduli of Intact Rock Core Specimens under Varying States of Stress and Temperatures, Annual Book of ASTM Standards, 2004.

[55] M.S. Diederichs, The 2003 Canadian geotechnical colloquium: mechanistic interpretation and practical application of damage and spalling prediction criteria for deep tunnelling, Can. Geotech. J. 44 (9) (2007 Sep) 1082–1116.
[56] A. Bobet, The initiation of secondary cracks in compression, Eng. Fract. Mech. 66 (2) (2000 May 1) 187–219.
[57] T.W. Lambe, R.V. Whitman, Soil Mechanics SI Version, John Wiley & Sons, New York, 2008.
[58] O. Tsoungui, D. Vallet, J.C. Charmet, Numerical model of crushing of grains inside two-dimensional granular materials, Powder Technol. 105 (1) (1999 Nov 1) 190–198.